The Effects of Defects on Localized Plating in Lithium-Ion Batteries

John Cannarella* **and Craig B. Arnold****,z**

Department of Mechanical and Aerospace Engineering, Princeton University, Princeton, NJ 08544, USA

This work investigates how local cell defects can induce local lithium deposition and dendrite growth in a lithium-ion cell that appears to otherwise be performing correctly. Using local pore closure in the battery separator as a model defect, we experimentally demonstrate the occurrence of local lithium deposition during cycling in coin cells containing deliberately manufactured local regions of separator pore closure. We further investigate the local plating phenomena observed in these experiments using an axisymmetric finite element model of the defect-containing coin cell geometry. Our simulations show that the pore closure acts as an "electrochemical concentrator," creating locally high currents and overpotentials in the adjacent electrodes. This leads to lithium plating if the local overpotential exceeds equilibrium potential in the negative electrode. We examine the sensitivity of the local plating behavior to various materials, geometric, and operating parameters to identify mitigation strategies. The results of this work can be generalized to any defect that creates spatially non-uniform current distributions.
 [DOI: 10.1149/2.1051507jes]

Manuscript submitted March 3, 2015; revised manuscript received April 15, 2015. Published April 28, 2015.

The formation of metallic lithium, or lithium plating, is a well-known and potentially dangerous degradation mechanism in lithium-ion batteries.[1] Lithium plating directly leads to capacity loss through corrosion with the cell's electrolyte[2] and in the worst case scenarios can lead to catastrophic failure by creating an internal short circuit.[1] Recent work shows a link between mechanics and lithium plating such that lithium plating is aggravated at higher levels of internal mechanical stress[3] and generally occurs in a periodic structure indicative of the cell's mechanical design.[3,4,5] However, the underlying physical mechanisms governing the relationship between lithium plating and mechanical stress remain unexplained. In this work we explain the observed link by experimentally demonstrating that local mechanical deformation of the battery separator can cause local lithium plating in an otherwise well-functioning cell. We support these experimental results with numerical simulations and an analytical analysis, which show that local separator deformation creates "hot spots" of locally high electrochemical activity that can cause local plating. While this work uses separator deformation as a model mechanical defect, the results are generally applicable to any defect that results in non-uniform ionic currents. Our results demonstrate the essential role of nonuniformities in causing failure in a seemingly well-functioning and well-designed battery cell, suggesting a new paradigm in which batteries are designed to be resistant to failure in the presence of an assumed pre-existing defect.

There are many known lithium-ion cell defects in addition to separator deformation that can result in spatially non-uniform internal operation.[6] Some examples of defects in lithium-ion cells include local electrolyte drying,[7] current collector delamination,[7] electrode/separator interface separation,[8] copper plating following overdischarge,[9] local regions of high tortuosity variation,[10] manufacturing defects,[11] and general mechanical deformation[12] or damage.[13] In this work we focus on the model defect of separator deformation because of its previous link to lithium plating,[3] as well as the ease with which a separator containing localized pore closure can be integrated into an experimental cell.[14] Separator deformation can be caused during the manufacturing process of the separator or of the battery cell, as well as during operation as a result of internal mechanical stress accumulation during charging[15–18] and aging.[19,3,20,21] The resulting mechanical deformation of the separator is understood to cause transport restrictions through a pore-closure mechanism,[22,14,23] which can occur in a spatially localized manner due to non-uniform mechanical stresses arising from the cell's architecture[24] as well as spatial variations in local electrode structure and mechanical properties.[10,25]

For such a defect to cause lithium plating locally within a battery cell electrode, the defect must cause the electrode's local electrochemical potential to drop below 0 V vs. Li/Li+.[26] This is a thermodynamic statement of the energetic favorability of metallic lithium formation: below 0 V, lithium formation is energetically favorable and plating is expected to occur. While this condition has not been previously linked to mechanical defects, it is well-known to occur during charging scenarios in which the the overpotential required for passing current exceeds the equilibrium potential of the negative electrode. Such scenarios include overcharge events in which the negative electrode is saturated with lithium,[27] fast charging in which high overpotentials are required to maintain high currents,[28] or low temperature charging in which higher overpotentials are required to compensate for slower kinetics.[29] Lithium plating is also known to occur locally near the edges of electrodes, where the local potential can drop below 0 V vs. Li/Li+ due to edge effects.[26] In this work we investigate the physical mechanisms by which mechanical defects in the battery separator can lead to lithium plating.

Experimental Observation of Defect-Induced Plating

To experimentally probe the effect of defects on lithium-ion cell operation, we assemble coin cells containing separators with deliberately manufactured regions of pore closure. The localized pore closure is produced by locally compressing the separator to produce a macroscopic region of closed pores, as shown in Figs. 1a and 1b, respectively. It is verified that this procedure produces closed pores through comparison of SEM images of the open and closed pore regions of the separator, shown in Figs. 1c and 1d. The electrodes and separator used in the coin cell are harvested from high quality commercial cells that have previously demonstrated good performance[3,19] to eliminate any possible defects due to poor electrode fabrication. A more detailed description of the methods and materials is provided in the Methods and materials section below.

The assembled cells are cycled between 2.7 V and 4.2 V at a C/2 rate according to manufacturer specifications and previous aging studies.[3,19] After cycling, we disassemble the cells and photograph the graphite electrodes, which provides an ex-situ visualization of the spatial distribution of lithium in the electrode due to the graphite color changes with lithiation. During lithiation, graphite progresses from black to red to gold, with gold indicating near-full lithiation.[30] This color progression can be seen in Figs. 2a and 2b , which show photographs of graphite electrodes taken from a charged and discharged cell, respectively. The electrodes in Figs. 2a and 2b are taken from cells containing pristine separators and show a uniform lithium

*Electrochemical Society Student Member.
**Electrochemical Society Active Member.
zE-mail: cbarnold@princeton.edu

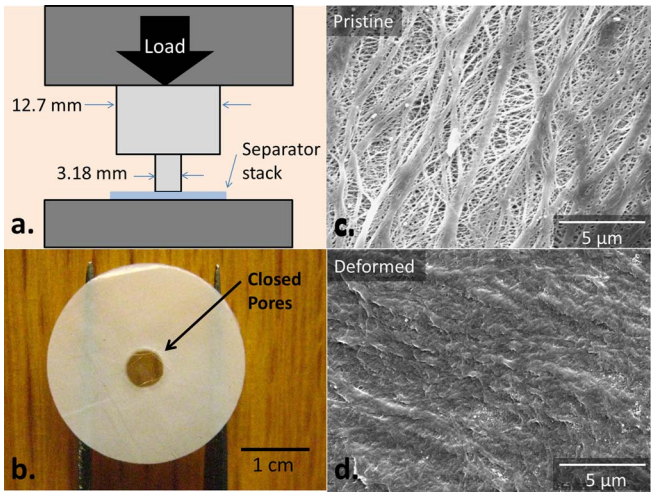

Figure 1. (a). Schematic of setup used to create localized separator pore closure through compressive deformation. (b). Photograph of separator after localized compression showing a region of local pore closure which appears transparent. (c). SEM image of an undeformed region of separator showing open pores. (d). SEM image of a deformed region of separator showing closed pores.

distribution based on graphite color and no lithium plating, as is desired in battery cell operation.

However, graphite electrodes taken from cells containing separator pore closure show spatially non-uniform color distributions indicative of heterogeneous current distribution during cycling. This can be clearly seen in Fig. 2c, which shows a graphite electrode taken from a cell containing a locally deformed separator after charging. The majority of the electrode surface is a red color, indicating a high lithium concentration. However, the region of the electrode surface that is in contact with the closed-pore region in the separators remains black, indicating that this region is under-utilized during charging and confirming the pore closure in the separator restricts transport.[22,23,14] A ring of gold-colored graphite can be seen separating the black and red regions, indicating locally higher lithium concentration in the graphite

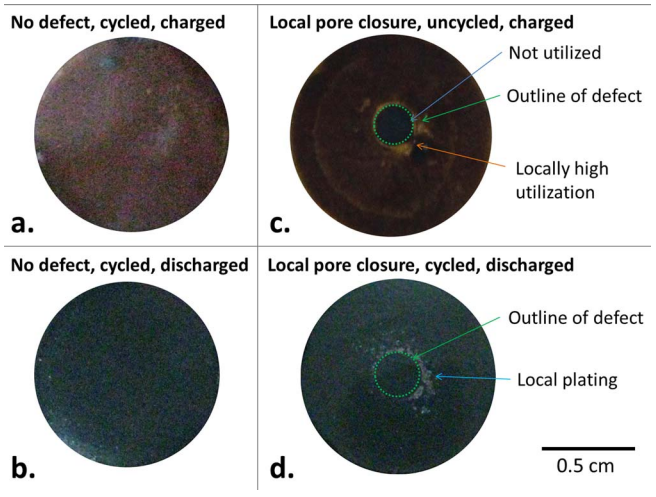

Figure 2. Graphite electrodes from a (a) charged defect-free cell after cycling showing uniform red color indicative of high lithium concentration and no plating, (b) discharged defect-free cell after cycling showing uniform gray color indicative of low lithium concentration and no plating, (c)defect-containing cell after first charge showing locally high utilization (gold color) caused by the defect and no observable plating, (d) discharged defect-containing cell after cycling showing local plating in a ring shape around the defect. The colors of the photographs have been enhanced to emphasize the spatial color variations.

electrode surface near the edge of the closed-pore region in the separator. This ring of gold-colored graphite is evidence that ion current through the separator is locally enhanced at the boundary between the closed and open pore region. The sharp interface between the gold and black colored graphite indicates that lateral transport along the plane of the graphite electrode is too slow to homogenize the lithium concentration within the electrode. Similar non-uniform distributions of lithium in the negative electrode have been observed in previous work due to separator pore closure during cycling[3] and due to deliberately manufactured transport restrictions.[8]

When the defect-containing cells are cycled, the formation of visible local lithium deposits adjacent to the region of local separator pore closure are frequently observed, as shown in Fig. 2d. The lithium deposits form in a ring around the region of pore closure, as might be expected based on the locally high-utilization evidenced by the photograph in Fig. 2c. The lithium deposits in Fig. 2d are deposits of so-called "dead lithium," which are deposits of lithium that are no longer electronically connected to the rest of the cell. We demonstrate this assertion in Fig. 2d by discharging the graphite electrode and observing that the lithium deposits still remain. If the lithium deposits were electronically connected to the graphite material, the lithium would be stripped during discharge or inserted into the graphite. These observations are consistent with previous observations of lithium deposition in cycled cells,[31,32] and provide experimental evidence that separator deformation can lead to failure/aging by causing local lithium plating. Furthermore, these results show that separator deformation can explain the link between lithium plating and mechanical stress, which is responsible for the spatially periodic nature of lithium deposits that is often observed in wound cells.[3–5]

Simulation of Defect-Induced Plating

Model description.— To better explain the physical mechanisms governing the localized plating behavior observed in our experiments, we conduct finite element simulations of the coin cells containing localized pore closure using the well-known Newman models implemented in COMSOL.[33,34,35,27,26] As done in previous work,[35,27] lithium plating kinetics are modeled as a side reaction using Butler-Volmer kinetics with an equilibrium potential of 0 V vs. Li/Li+ and the plated film thickness is calculated by integrating the plating flux over time. The governing equations are summarized in Appendix B; only the elements of the model that are unique to this work are described in this section.

Fig. 3 shows the geometry and mesh used in this simulation, which is a 2D axisymmetric representation of a coin cell containing a concentric circular region of closed pores in the separator. During simulation, higher gradients form near the open-closed pore interface, so we

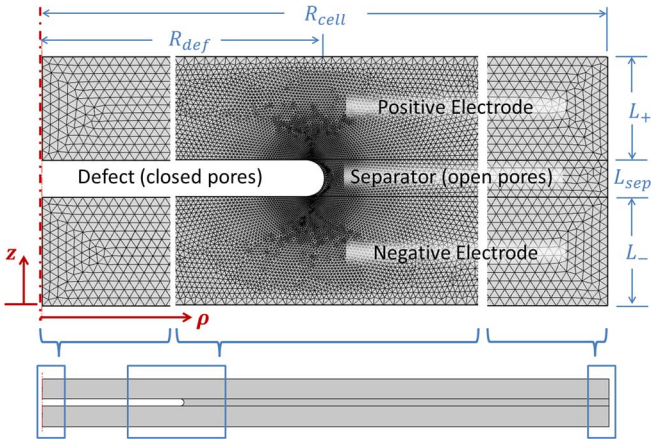

Figure 3. Schematic showing the axisymetric geometry and corresponding mesh used in the simulations.

Table I. Table of parameter values used in the baseline simulation.

Electrode and Separator Domain Properties

Parameter	Negative	Separator	Positive
L_i (m)	7.35×10^{-5}	2.5×10^{-5}	7.0×10^{-5}
R_i (m)	1.25×10^{-5}	-	8.5×10^{-6}
ϵ_s	0.505	0.55	0.55
ϵ_l	0.438	0.45	0.3
$brug$	4.1	2.3	1.5
U_i (V vs. Li/Li+)	Eq. C6	-	Eq. C5
$c_{s,max}$ (mol/m^3)	31858	-	49943
$c_{s,min}$ (mol/m^3)	0	-	20976
$D_{s,bulk}$ (m^2/s)	2.58×10^{-14}	-	10^{-11}
$\kappa_{s,bulk}$ (S/m)	100	-	10
k_1 (m/s)	1.76×10^{-11}	-	6.67×10^{-11}
α_a, α_c	0.5	-	0.5

Electrolyte Properties

Parameter	Value
$\kappa_{l,bulk}$ (S/m)	Eq. C2
$D_{l,bulk}$ (m^2/s)	Eq. C1
v	Eq. C3
t_+	0.435
$c_{l,0}$ (mol/m^3)	1000

Cell Properties

Parameter	Value
γ	0.06325
SOH_{init}	0.9
R_{def} (m)	5×10^{-4}
R_{cell} (m)	2×10^{-3}
SOC_{init}	0.05

refine the mesh near this interface as shown in Fig. 3. The simulation is conducted using 30s time steps with initially smaller steps at the beginning of the simulation. It is verified that further refinement of the mesh and time steps produce the same results. The model is parameterized using the independent parameters of positive electrode thickness L_+, excess negative electrode capacity γ, state of health SOH, state of charge SOC, and C-rate. These parameters are used to determine the negative electrode thickness L_-, initial average lithium concentrations in each electrode, and charging current. The C-rate is defined on the basis of areal capacity adjacent to open pores of the cell. This C-rate definition is made so that the current in the bulk ($\rho \gg R_{def}$) does not depend on the size of the defect, which would generally be the case in a cell where the defect is relatively small. Mathematical formulations of the above discussion are presented in Appendix B.

The cell simulated in this work is based on the the cell reported in Ref. 36. We choose to simulate this cell because it is qualitatively similar to the cell used in our experimental work, both in terms of materials, geometry, excess negative electrode capacity, and initial SOH, and because this cell has been previously demonstrated to be well-described by the models used in this work.[36,37] Further attempts on establishing quantitative agreement between the model and experiment is beyond the scope of this work and provides little extra insight into the fundamental mechanisms underlying lithium plating in the presence of a defect, as at present it is difficult to accurately quantify lithium plating both experimentally and theoretically. One major challenge in this area is that only lithium that is electronically disconnected from the graphite (so-called "dead lithium") can be observed ex situ; electronically connected lithium is expected to insert into the underlying electrode prior to disassembly.[38,31,32] However, the formation process of dead lithium is still poorly understood,[1] preventing its meaningful inclusion in the present model. The cell parameters used in this simulation are tabulated in Table I, and are the same as those reported in Ref. 36. All temperature dependent parameters are evaluated at 298 K and a 4.1 V voltage cutoff is used to determine the end of charging.[36] The concentration-dependent electrode equilibrium potential curves used in this work are taken from the empirical relations reported in Ref. 26, as similar expressions are not included in Ref. 36. Plots and empirical relations for the concentration-dependent parameters used in this work are provided in Appendix C.

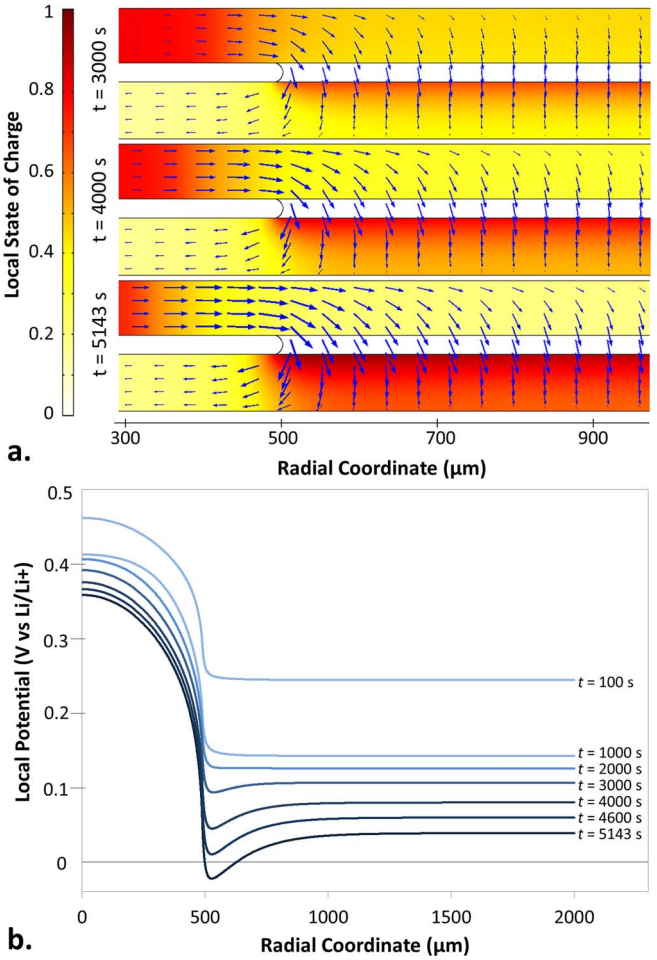

Figure 4. (a.) Results from simulation at three different times showing local soc distribution in both electrodes. Arrows are overlaid indicating the direction and relative magnitude of electrolyte current in the cell. After around 3,000 seconds, the lateral current in the positive electrode exceeds the lateral current in the negative electrode, accumulating Li near the open/closed pore interface. (b.) Plot of local negative electrode potential (vs. Li/Li+) as a function of radial coordinate along the separator/negative electrode interface. After around 3,000 seconds of charging, the potential profile begins to exhibit local enhancement.

Simulation results.— The results from numerical simulations of defect-containing coin cells provides a wealth of insight into the observed localized phenomena that would be difficult to determine experimentally. The tendency of the local pore closure to create locally high currents and utilization in the vicinity of the interface between open and closed pores can clearly be seen in Fig. 4. Fig. 4 shows the local solid phase lithium concentration at the electrode particle surface with arrows overlain to indicate the magnitude and direction of the ion current. The arrows indicate the direction in which the electrolyte current vector is pointing and the relative sizes of the arrows qualitatively indicate the magnitude of the electrolyte current. The solid phase lithium concentration in each electrode is presented as local state of charge as function of radial coordinate ρ and axial coordinate z:

$$soc(\rho, z) = \frac{c_{s,surface} - c_{s,min}}{c_{s,max} - c_{s,min}} \quad [1]$$

where $c_{s,surface}$ is the local solid-phase surface concentration of lithium, and $c_{s,min}$ and $c_{s,max}$ are the minimum and maximum concentration limits of lithium in the solid-phase electrode material specified in Table I.

Fig. 4 a shows that during charging, the negative electrode is locally over-utilized near the open/closed pore interface in the separator, with

the graphite in this region approaching its maximum concentration of lithium, in agreement with the experimental observations in Fig. 2c. This local over-utilization can be seen to occur as a result of a net accumulation arising from unequal lateral (ρ direction) ion transport in the positive versus negative electrodes. The lateral transport is higher in the positive electrode than the negative for two reasons. The first is due to the nature of the equilibrium potential curves of each electrode material. The positive electrode equilibrium potential shows a much higher concentration dependence than does the negative electrode (see Appendix C). This concentration dependence means that within a single electrode, regions of high lithium concentration undergo oxidation (Li dissolution) more rapidly than regions of low lithium concentration. This creates a corrosion-type process within a single electrode in which lithium transport from lithium rich to lithium deficient regions is enhanced by non-uniform reaction rates. In the case of the particular cell under consideration, lateral transport through the negative electrode is also impeded by a higher tortuosity compared to the positive electrode.[36]

The locally-enhanced electrochemical operation in the vicinity of the pore closure seen in Fig. 4a causes a drop in local potential during charging as shown in Fig. 4b. The quantity plotted in Fig. 4b is the local potential with respect to a lithium reference electrode in the negative electrode, V_-, measured at the separator-negative electrode interface. V_- is equal to the local electrode equilibrium potential U_- (which is referenced against Li/Li+) plus the insertion reaction overpotential η_-, which is equivalent to the difference between the local solid and liquid phase potentials, ϕ_s and ϕ_l:

$$V_- = \phi_{s,-} - \phi_{l,-} = U_- + \eta_- \quad [2]$$

Fig. 4b shows that for the baseline case of C/2 charging, the graphite electrode develops a locally lower potential with respect to the bulk ($\rho \gg 500\mu m$) of the electrode after 2000 seconds of charging. After 4600 seconds of charging, this local potential begins to locally dip below zero at the open/closed pore interface, indicating that local lithium deposition is thermodynamically favorable. The magnitude of this local depression in potential increases during the remainder of charging until the cell reaches its 4.1 V charging cutoff after 5143 seconds. In simulations in which we consider the addition of a subsequent constant-voltage charging step (as would be used in a typical constant-current, constant-voltage charging scheme), we find that the local potential in the negative electrode rapidly relaxes (increases) toward its equilibrium value. Thus the local potential at the end of constant-current charging represents a local minimum with respect to time. Because the potential relaxes quickly during a subsequent constant-voltage step, the constant voltage step contributes little additional lithium deposition and is consequently not presented in this work.

The plated lithium film thickness at the separator interface of the graphite electrode is plotted as a function of radial coordinate in Fig. 5a. Three film thicknesses are plotted based on the results of simulations conducted assuming a lithium deposition exchange current of 10, 20, and 30 A/m^2, as has been done similarly in previous work because of the range of exchange current densities reported in the literature.[35,27] The resulting films form a ring shape around the pore closed area on the negative electrode surface, which is visualized in three dimensions for the 10 A/m^2 case in Fig. 5b. This localized lithium deposition is likely to result in increased localized stress, as it has previously been observed that lithium deposition can cause measurable changes in cell thickness.[39,40] This local increase in stress could lead to further separator deformation, creating a potential positive feedback scenario in which defects grow. Similarly, if the lithium deposit becomes electronically disconnected from the underlying graphite (as is often observed experimentally,[3,4,5,1,38]) the dead lithium deposit itself becomes a defect, restricting transport in the same manner as separator pore closure. These two growth mechanisms can explain the relatively large local lithium deposits observed in experiments.

The simulated values of these film thicknesses should be regarded as only a crude estimate, as the kinetics of lithium deposition on

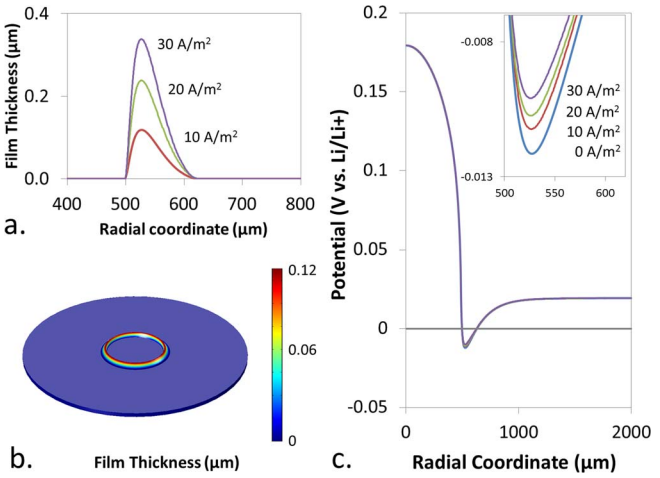

Figure 5. Plated lithium film thickness at end of charging (a) plotted as a function of radial coordinate at the separator/negative electrode interface and (b) represented three-dimensionally for the case of a 10 A/m^2 plating exchange current. (c.) Plots of the local potential (zoomed inset) at the end of charging as a function of radial coordinate at the separator/negative electrode interface showing little variation with assumed plating exchange current value.

graphite electrodes are still poorly understood. The kinetic model used here and in previous work[35,27] does not consider insertion of lithium from the film deposit into the underlying graphite material, which is known to occur experimentally.[38] Furthermore, in the model, lithium deposition and lithium insertion from the electrolyte occur simultaneously, whereas in reality, no lithium deposition from the electrolyte should be able to occur after the formation of a lithium film. These two errors are likely to be offsetting to some extent, and more accurate inclusion of these effects requires fundamental experimental study outside the scope of this present work.

The inclusion of lithium plating kinetics and variation of the corresponding plating exchange current is expected to alter the local potential with respect to a lithium reference. This effect can be seen in Fig. 5c, which shows the local potential at end of charging from simulations conducted assuming 0 (no plating), 10, 20, and 30 A/m^2 lithium plating exchange current. Unlike the plated lithium film thickness, the local potential is relatively insensitive to the value of exchange current, shifting positive by only a slight amount with increasing exchange current. Because of this relative insensitivity, in the remainder of this work we focus on local potential as a measurement of the effects of localization and plating, with an assumed plating exchange current of 10 A/m^2.

Parametric analysis.— To gain better insight into the sensitivity of the simulated defect-induced voltage localization to various design parameters and materials properties, we present a sensitivity analysis in Fig. 6. The sensitivity analysis is conducted by varying the paramter of interest by +/− 10% and measuring the effect on local potential after 4000s of charging. An example for the case of a sensitivity analysis on negative electrode porosity is shown in Fig. 6 a, which shows that higher negative electrode porosities result in decreased localization as measured by ΔV marked on the chart, as well as an overall higher local potential in the electrode. To succinctly quantify the results in Fig. 6a as well as the localization sensitivity to variation in other parameters, we define a sensitivity parameter χ as the percent change in localization per percent change in a given parameter:

$$\chi = \frac{\Delta V_{+10} - \Delta V_{-10}}{\Delta V_0 \cdot 0.2} \quad [3]$$

Parameters associated with large positive or negative values of χ in Fig. 6b indicate parameters that strongly increase localization as they are increased or decreased, respectively. Parameters with values

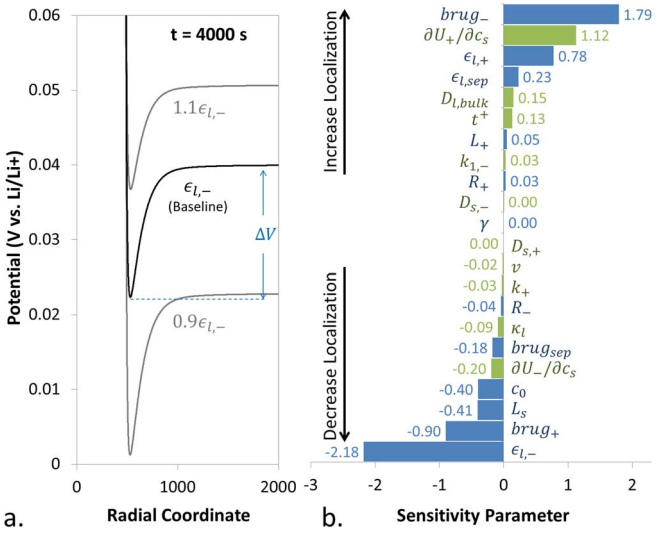

Figure 6. (a.) Example of voltage curves after 4000s of charging used in the sensitivity analysis of negative electrode porosity $\epsilon_{l,-}$ showing a reduction in ΔV with an increase in $\epsilon_{l,-}$. (b.) Summary of calculated χ values from sensitivity analysis results with design parameters in blue and materials properties in green. More positive/negative values indicate that localization increases/decreases with a corresponding increase in a given parameter.

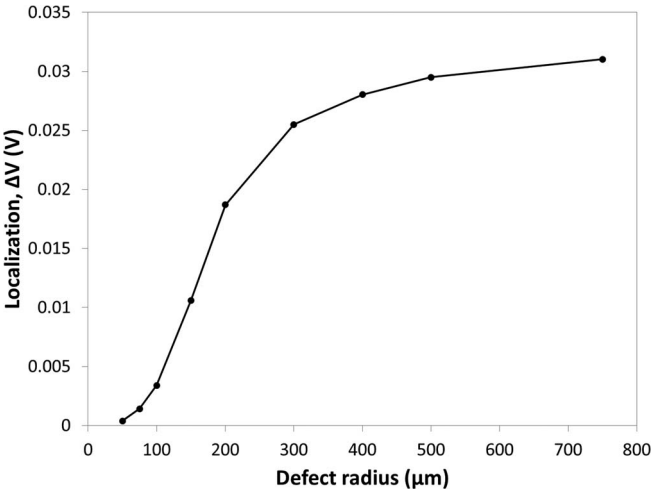

Figure 7. Plot of localization in terms of ΔV as a function of defect radius showing that localization does not occur for defects under ~100 μm in the simulated cell.

approaching 0 have little effect on localization, even though they may have a strong effect on the absolute value of the local potential.

The general trend seen in Fig. 6b is that modifications to the cell design that improve ion transport in the negative electrode relative to the positive electrode help to mitigate the localization effects of defects. For example, design modifications that enhance ion transport in the negative electrode such as increasing porosity $\epsilon_{l,-}$ or decreasing Bruggeman exponent $brug_-$ (i.e. decrease tortuosity) result in lower degrees of localization. Similarly, restricting ion transport in the positive electrode (i.e. decrease $\epsilon_{l,+}$, increase $brug_+$) also mitigates the degree of localization occurring in the negative electrode. The slopes of the equilibrium potential curves $\frac{\partial U}{\partial c_s}$ can also impact the overall transport of ions within the electrodes by providing an electrochemical driving force for smoothing out concentration gradients, with steeper slopes providing higher driving forces. In principle, this means that some materials are inherently "safer" than others with respect to localized phenomena. It is also important to note that in developing localization mitigation strategies, some parameters can be varied to a much greater extent than others, representing a greater potential utility in reducing localization. For example, although $\frac{\partial U_-}{\partial c_s}$ has a relatively low sensitivity, it has no upper limit and can therefore be increased many times beyond +10%, thus providing a potentially effective strategy for localization reduction. A more fundamental discussion of the effects of each parameter on localization is presented in the next section.

One question of practical importance is the minimum defect size for which voltage localization is expected. To address this question we conduct simulations in which we vary the size of the defect and observe its effect on localization, as shown in Fig. 7. Fig. 7 shows that for the baseline cell, localization begins to decrease rapidly below defects of radius 300 μm, and no significant localization occurs below a defect radius of under ~100 μm. This suggests that unexpected failure due to defect-induced lithium plating can be avoided by appropriate inspection of battery cells for macroscopic defects with length scales above 100 μm, thereby increasing the reliability and safety of lithium-ion energy storage systems. In practice this could be achieved prior to assembly by monitoring individual cell components,[11] or after assembly through nondestructive techniques such as X-ray[12] or ultrasound analysis.[41,42]

Analytical explanation of results.— The previous section showed how local defects such as separator pore closure create hot spots that can result in local lithium deposition. In this section we explain more fundamentally the reasons for the local variation in potential responsible for the lithium plating as well as observations made in the sensitivity analysis from the previous section. To understand the variations in local potential, it is necessary to first understand the relation of local potential to the more familiar (and easier to measure) cell potential. The cell potential V_{cell} can be written as

$$V_{cell} = \phi_{s,+} - \phi_{s,-} = U_+ - U_- + \eta_+ - \eta_- + \phi_{l,+} - \phi_{l,-} \quad [4]$$

which must be satisfied by any two points "+" and "−" within the positive and negative electrode, respectively. This equation assumes that variation in ϕ_s is negligible in each electrode, which is a valid assumption for well-made battery cells with sufficient conductive additive. Consequently, V_{cell} is spatially constant, and equal to 4.1 V at the end of charge, as dictated by the charging scheme. This expression can be rearranged to give an expression for the local potential of the negative electrode with respect to a lithium reference:

$$V_- = U_- + \eta_- = U_+ + \eta_+ + \Delta\phi_l - V_{cell} \quad [5]$$

where $\Delta\phi_l$ is the difference in liquid phase potential between the + and − points. Lithium deposition is expected to occur when this local potential is less than 0 V vs. Li/Li+, the equilibrium potential of the lithium deposition reaction. We can express this criterion by setting the left hand side of Eq. 5 to 0:

$$U_+ + \eta_+ + \Delta\phi_l - V_{cell} < 0 \quad [6]$$

If the above criterion is satisfied between any two points in the positive and negative electrode, lithium deposition is expected to occur. This criterion can be used to qualitatively reason why deposition occurs near the open/closed pore interface in the previous simulations. The $\Delta\phi_l$ term on the left hand side indicates that deposition is expected to occur near the interface of the open pore separator region and negative electrode, as this represents the location with the smallest voltage drop in the electrolyte phase. This conclusion follows intuitively, and has been seen in previous work where lithium deposition occurs only near the separator interface.[27]

The U_+ term governs the radial location for which we would expect lithium deposition. Lithium deposition would be expected to be more favorable at locations along the negative electrode that are adjacent to regions with a lower U_+. This is equivalent to saying that lithium deposition is more favorable adjacent to regions of the positive electrodes with locally high lithium concentration, as equilibrium potential generally decreases with higher lithium concentration. During

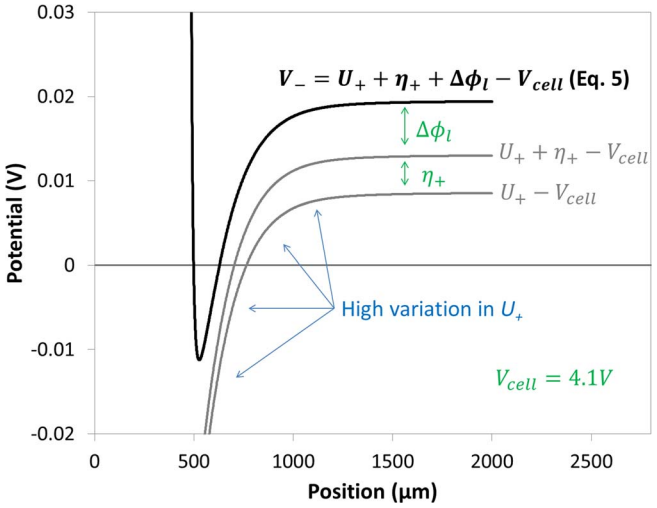

Figure 8. Plot of relevant potentials from eqns. 4-6 as a function of radial coordinate at end of discharge. This plot shows that the local depression in potential in the negative electrode can be understood by considering the local depression in equilibrium potential in the opposing positive electrode.

charging in the presence of a defect, the solid phase lithium concentration in the positive electrode is higher adjacent to the defect where the cell is under-utilized, and plating is expected at radial locations near the defect. Combining these two observations, we expect to find plating at the separator/negative electrode interface adjacent to the defect, which agrees with the simulation results presented in Fig. 5. Note that in this brief analysis, we have ignored possible variation in η_+ or radial variation in $\Delta\phi_l$, as these two terms are small relative to the others.

To better understand the previous discussion, we can plot the potentials of interest in both electrodes at the separator interface as a function of radial location in the cell as shown in Fig. 8. This plot shows that the radial variation in local potential vs. Li/Li+ in the negative electrode is due primarily to a corresponding variation in the equilibrium potential of the positive electrode on the other side of the separator. This can be seen through the high spatial variation in the $U_+ - V_{cell}$ curve, which can be attributed entirely to spatial variation in U_+ because V_{cell} is constant as discussed previously. It can also be seen that variation in η_+ and $\Delta\phi_l$ are relatively small, supporting previous assumptions. The large variation in positive electrode equilibrium potential is due to the high $\frac{\partial U}{\partial c_s}$ in the positive electrode multiplied by a relative increase in local solid phase concentration near the defect:

$$U_{+,loc} = U_{+,bulk} + \frac{\partial U_+}{\partial c_s}(c_{s,loc} - c_{s,bulk}) \quad [7]$$

The "loc" and "bulk" subscripts are added to Eq. 7 to distinguish between local values near the defect and bulk values unaffected by the defect due to distance. Eq. (7) shows that it is a combination of $\frac{\partial U}{\partial c_s}$ and the local solid phase lithium concentration $c_{s,loc}$ that primarily determines the magnitude of localization in potential. It follows that the local change in potential depends in part on the parameters that determine the lateral current around the defect in either electrode, as lateral transport rates determine the degree of localization in lithium concentration. This can be understood by analyzing the charge balance equation from concentrated solution theory reproduced below assuming one-dimensional transport in the lateral ρ direction.

$$-i_l = \kappa_l \frac{\partial \phi_l}{\partial \rho} + \frac{2RT\kappa_l}{F}\frac{v}{c_l}\frac{\partial c_l}{\partial \rho} \quad [8]$$

The liquid phase conductivity κ_l can be written as $\kappa_l = \epsilon_l^{brug}\kappa_{l,bulk}$, which shows that conductivity depends on design parameters porosity ϵ_l and tortuosity (as dictated by the *brug* exponent), as well as bulk ionic conductivity $\kappa_{l,bulk}$. We can also make a simplifying assumption that $\frac{\partial \phi_l}{\partial \rho} = \frac{\partial U_i}{\partial \rho}$ to see how the concentration dependence of the equilibrium potential affects lateral transport:

$$-i_l = \epsilon_l^{brug}\kappa_{l,bulk}\frac{\partial U_i}{\partial c_s}\frac{\partial c_s}{\partial \rho} + \frac{2RT\epsilon_l^{brug}\kappa_{l,bulk}}{F}\frac{v}{c_l}\frac{\partial c_l}{\partial \rho} \quad [9]$$

This simplification is equivalent to assuming that spatial variations in overpotential are small relative to the spatial variations in equilibrium potential. This assumption is reasonable for the positive electrode where overpotentials are small, but less so for the negative electrode. Nevertheless, it is useful for understanding the relevant physics.

From Eq. 9, a number of important parameters that govern lateral transport emerge. First, the variation in equilibrium potential with solid phase concentration $\frac{\partial U_i}{\partial c_s}$ plays a role in determining lateral transport, in addition to its effect on potential seen in Eq. 7. Eq. 9 also shows that the porosity and tortuosity (bruggeman correction) of each electrode are critical in determining lateral transport rates. Localization is particularly sensitive to these parameters because they are specified independently in each electrode, and it is the relative rates of lateral transport that determine localization. This is in contrast to the electrolyte properties that appear in Eq. 9 which cannot be independently varied in each electrode, and consequently have a smaller effect on localization. Note that while porosity/tortuosity is assumed to be isotropic in this work, it is interesting to note that other work has shown a strong directional anisotropy, which could have a significant effect when considering lateral transport in a cell.[43,44] The conclusions of this analytical analysis agree with the simulated sensitivity in Fig. 6, providing a more fundamental understanding of how cell design parameters and materials properties affect localization.

This understanding can be used to create a rational framework for the development of safer and longer lasting lithium-ion cells that are designed to mitigate defect-induced lithium plating. For example, the porosity and tortuosity of each electrode can be altered in each electrode to achieve improved resistance to localization. Exploiting directional anisotropies in these transport properties can allow for the radial direction properties to be altered independently of the axial direction properties, allowing for localization effects to be mitigated without altering desired axial transport properties. Decreasing tortuosity is particularly desirable, because unlike increasing porosity, decreasing tortuosity does not necessarily reduce the energy density of the cell. Beyond electrode design, these results also suggest that certain materials should be safer with respect to lithium plating than others. For example, positive electrode materials with low-sloped equilibrium potential curves with respect to solid-phase lithium concentration–especially near end of charging–are expected to significantly reduce localized electrochemical phenomena. In applications where safety and reliability are more important than energy density, using negative electrodes with sloped equilibrium potential curves may also be a desirable solution.

Conclusions

This work shows through a combination of experiment and simulation that local defects can create hot spots of locally high electrochemical activity that can lead to lithium plating. These observations provide a mechanistic link between electrochemical degradation/failure and internal mechanical stress in lithium-ion batteries, whereby mechanical stress creates or aggravates defects such as separator pore closure. The results of this work should be generally applicable to any defects that result in local transport restrictions, such that any general macroscopic defect occurring in a cell might be expected to cause unanticipated lithium plating. Defects that completely eliminate lateral transport in the negative electrode, such as delamination of the negative electrode from the current collector, might be expected to exhibit even more pronounced localized phenomena. The numerical and analytical analyzes presented in this study provides a first step in understanding how to mitigate the effects of defects in cell design, which may unexpectedly arise from a multitude of sources. While this work

focuses on lithium plating in the negative electrode during charging, the analysis presented in this work could also be applied to any other degradation mechanism that depends on local electrochemical conditions such as electrolyte oxidation in the positive electrode during charging. The implications of these analyzes is that battery cells can be designed with higher safety, reliability, and life, by considering the effects of defects in cell design and materials selection. Furthermore, these results suggest that inspecting batteries for macroscopic defects could be a viable strategy for providing early warning of potential failure in battery storage systems.

Acknowledgments

J.C. acknowledges the Department of Defense (DoD) for support through the National Defense Science and Engineering Graduate Fellowship (NDSEG) Program. We acknowledge support from the Princeton University Siebel Energy Grand Challenge and the Princeton University Carbon Mitigation Initiative. We also acknowledge the Rutgers-Princeton NSF IGERT in Nanotechnology for Clean Energy.

Appendix A: Methods and Materials

The electrode and separator materials used in the experimental section are harvested under argon atmosphere (< 0.1 ppm O_2 & H_2O) from pristine commercial pouch cells, which have been used and described in prior publications.[3,19] The harvested polyethylene separator is rinsed in dimethyl carbonate (DMC) and punched into 1.43 cm diameter disks. A stack of separator disks usually containing between 10 and 30 separator layers are then transferred to a compression testing machine to be locally deformed through the application of a local compressive mechanical stress, which has been shown to cause pore closure in separators.[14] The compression testing machine is fitted with a 5kN load cell and spherically seated platens to maintain good alignment. The separator disks are wetted with DMC to accelerate the separator deformation, as DMC immersion is known to weaken the mechanical properties of battery separators.[45–49] A custom ram shown schematically in Fig. 1a is used to apply a localized compressive stress in a 3.18 mm diameter region near the center of the separator disk. The applied stress is 60 MPa for 7 hours, which results in the pore closure shown in Fig. 1b and 1d. An SEM image of the pristine pore structure is shown in Fig. 1c for reference. The deformed separators are then dried and transferred to the argon atmosphere for coin cell assembly.

Lithium cobalt oxide positive and graphite negative electrodes are harvested from the same commercial pouch cell as the separators. Prior to disassembly, the pouch cell is discharged to its lower voltage cutoff of 2.7 V such that coin cells assembled with the harvested electrodes are initially at a state of charge near zero. One side of the double sided electrodes is removed by carefully scraping off the electrode material to expose the current collector. The scraped electrodes are then punched into 1.11 cm diameter disks for the positive electrode and 1.27 cm diameter disks for the negative electrode. The negative electrodes, positive electrodes, and separator disks are all soaked in separate containers of 1M $LiPF_6$ in EC/DMC (1:1 by weight) electrolyte prior to assembly to ensure they are fully wet. We have observed that skipping this wetting step can lead to the formation of bubbles between the electrodes after coin cell assembly, which adversely affects cell performance. The coin cells are then transferred to ambient atmosphere where they are cycled.

The coin cells are cycled using a CCCV charging procedure and a constant current discharge procedure between 2.7 V and 4.2 V. The cutoff current during the constant voltage step is set to a C-rate of C/3. For defect-containing cells, the C-rate is multiplied by a factor of 0.92 to account for the reduction in accessible capacity in the areas of the electrodes adjacent to the defect. The cells are cycled for 300 cycles at the specified current and then transferred to argon atmosphere for disassembly. The cycled coin cells are disassembled using a commercial coin cell disassembler and photographed.

Appendix B: Summary of Model Equations

The governing equations underlying the Newman models are described in detail in many previous works.[33,34,35,27,26] The relevant equations are summarized briefly here for the reader's reference. Symbol definitions and values are tabulated in Table B1.

Liquid phase equations.— The liquid phase is governed by statements of conservation of mass:

$$\epsilon_l \frac{\partial c_l}{\partial t} = \nabla \cdot (\epsilon_l D_l \nabla c_l) + a \left(1 - t^+\right)(j_1 + j_2) \quad [B1]$$

and conservation of charge in the electrolyte:

$$\nabla \cdot \left(-\kappa_l \nabla \phi_l + \frac{2\kappa_l RT}{F} v \nabla \ln c_l\right) = i_l \quad [B2]$$

Table B1. Table of symbols and their corresponding definitions and dimensions.

Symbol	Definition
	Parameters
a	specific interfacial area of electrode (m^2/m^3)
$brug$	Bruggemann exponent factor
c_i	Li concentration in phase i (mol/m^3)
$D_{i,bulk}$	Bulk diffusion coefficient in phase i (m^2/s)
D_i	Diffusion coefficient corrected for porosity and tortuosity
F	Faraday's constant (96487 C/mol)
i_i	Current density in phase i (A/m^2)
I_{app}	Applied current density (A/m^2)
j_i	Rate of surface reaction i ($mol/m^2/s$)
k_i	Rate constant of reaction i (m/s)
L_i	Thickness of domain i (m)
M_{Li}	Molecular weight of lithium (0.00694 kg/mol)
R	Ideal gas constant (8.314 J/mol/K)
R_{cell}	Cell radius (m)
R_{def}	Defect radius (m)
R_i	Particle radius in domain i (m)
soc	Local state of charge
SOC	Cell state of charge
SOH	Cell state of health
t^+	Cationic transference number
T	Temperature (K)
U_i	Open-circuit potential of electrode material in domain i (V vs. Li/Li+)
v	Electrolyte thermodynamic factor
V	Local potential (V vs. Li/Li+)
V_{cell}	Cell voltage (V)
x, y	Stoichiometric coefficients
α_a, α_c	Anodic, cathodic transfer coefficient
γ	Excess capacity
δ_{film}	Li surface film thickness (m)
ϵ_i	Volume fraction of phase i
η_i	Overpotential of reaction i(V)
$\kappa_{i,bulk}$	Bulk ionic/electronic conductivity of phase i (S/m)
κ_i	Conductivity of phase i corrected for porosity and tortuosity (S/m)
ρ_{Li}	Density of lithium metal (kg/m^3)
ϕ_i	Potential of phase i(V)
	Coordinates
r	Particle radial coordinate (m)
ρ	Cell radial coordinate (m)
z	Cell axial coordinate (m)
ψ	Cell azimuthal coordinate (m)
t	Time (s)
	Subscripts
l	liquid phase
s	solid phase
$+$	positive electrode domain
$-$	negative electrode domain
sep	separator domain
$cell$	entire cell
1	insertion reaction
2	plating reaction

Here v is a concentration and temperature dependent thermodynamic factor that is calculated based on the empirical correlation in Eq. C3. The specific surface area a is calculated assuming spherical particles. Because the liquid phase exists in a porous medium, property corrections must be made for both liquid phase diffusion coefficients

$$D_l = D_{l,bulk}\epsilon_l^{brug} \quad [B3]$$

and ionic/electronic conductivity

$$\kappa_i = \kappa_{i,bulk}\epsilon_i^{brug} \quad [B4]$$

No flux and no current conditions are imposed at all external boundaries and closed-pore boundaries:

$$\nabla_n c_l = 0 \quad [B5]$$

$$\nabla_n \phi_l = 0 \quad [B6]$$

where ∇_n indicates a directional derivative along the surface normal.

Solid phase equations.— In the solid phase, electric current is governed by Ohm's law:

$$i_s = -\kappa_s \nabla \phi_s \quad [B7]$$

The divergence of current in the solid phase is coupled to the divergence of current in the liquid phase through reaction fluxes j_i:

$$\nabla \cdot i_s = -\nabla \cdot i_l = -aF\,(j_1 + j_2) \quad [B8]$$

Here j_1 is the flux due to the lithium insertion reaction

$$j_1 = k_1 c_l^{\alpha_{a,1}} (c_{s,max} - c_s)^{\alpha_{a,1}} c_s^{\alpha_{c,1}} \left(\exp\left(\frac{\alpha_{a,1} F}{RT} (\phi_s - \phi_l - U) \right) - \exp\left(-\frac{\alpha_{c,1} F}{RT} (\phi_s - \phi_l - U) \right) \right) \quad [B9]$$

where U is the concentration-dependent equilibrium potential of the electrode material plotted in Fig. 10. The plating reaction flux j_2 is given by Eq. B10 using Butler-Volmer kinetics as done in previous work,[35,27]

$$j_2 = \frac{i_{0,2}}{F} \left(\exp \frac{\alpha_{a,2} F}{RT} \eta_2 - \exp \frac{-\alpha_{c,2} F}{RT} \eta_2 \right) \quad [B10]$$

$$\eta_2 = \phi_s - \phi_l \quad [B11]$$

Parameters associated with the deposition reaction are specified with the subscript "2," while parameters associated with the lithium insertion reaction are specified with the subscript "1." The accumulation of lithium on the particle surface can be accounted for by tracking the change in the lithium film thickness δ_{film} over time. This thickness depends on the lithium deposition flux onto the surface and the molecular weight M_{Li} and density ρ_{Li} of lithium metal:[35,27]

$$\frac{\partial \delta_{film}}{\partial t} = -\frac{j_2 M_{Li}}{\rho_{Li}} \quad [B12]$$

Insulating conditions are imposed at closed pore boundaries and at $\rho = R_{cell}$ such that

$$\nabla_n \phi_s = 0 \quad [B13]$$

At the negative current collector ($z = 0$), ϕ_s is arbitrarily set to 0. A current is applied at the positive current collector boundary ($z = L_- + L_{sep} + L_+$) such that

$$\int_{\partial\Omega} i_z dl = I_{app} \int_{\partial\Omega} dl \quad [B14]$$

The above integral is understood to be appropriately evaluated over the circular area defined by R_{cell}. This statement of current along the boundary allows the imposed current to vary spatially with the constraint that the spatially-averaged current density be equal to I_{app}. I_{app} is specified in terms of C-rate, which is commonly defined for a battery cell such that a "N" C-rate is the current required to discharge a cell in 1/N hours (e.g. 2 hours for a 0.5C rate). I_{app} is thus equal to $I_{app,1C}$ multiplied by the C-rate, where $I_{app,1C}$ is given by

$$I_{app,1C} = \frac{F \Delta c_+ L_+ \epsilon_+}{3600} \frac{R_{cell}^2 - R_{def}^2}{R_{cell}^2} \cdot SOH \quad [B15]$$

This C-rate definition excludes capacity contributions from electrode material directly adjacent to the closed pores. That is, capacity contributions from electrode material located between $0 < \rho < R_{def}$ are excluded. The modification by the geometric factor is necessary for the specification of C-rate in this simulation because the pore closure accounts for a significant area fraction of the simulated cell. Modifying the C-rate by the geometric factor makes the C-rate the same current density that would be present in a cell for which the pore closure is highly localized and accounts for a relatively insignificant fraction of the area. This can be verified by observing that when $R_{cell} \gg R_{def}$, the C-rate definition approaches what one would expect for a defect-free cell.

Particle pseudo dimension.— The electrode particles are treated as a pseudo dimension with spatial coordinate r denoting radial location within a spherical particle.[27] Within the particle, diffusion of lithium is governed by Fick's laws

$$\frac{\partial c_s}{\partial t} = \nabla \cdot (-D_s \nabla c_s) \quad [B16]$$

with the following boundary conditions at $r = 0$:

$$\frac{\partial c_s}{\partial r} = 0 \quad [B17]$$

and at $r = R_i$

$$-D_s \frac{\partial c_s}{\partial r} = j_1 \quad [B18]$$

Axisymmetric boundary conditions.— Axisymmetric boundary conditions are imposed in the solid and liquid phases such that there is no variation in the azimuthal direction:

$$\frac{\partial X}{\partial \varphi} = 0 \quad [B19]$$

and no flux across the axis of symmetry at $\rho = 0$:

$$\frac{\partial X}{\partial \rho} = 0 \quad [B20]$$

Here X is an arbitrary variable (e.g. concentration or potential).

Constrained model parameters.— The thickness of the electrodes are constrained such that the thickness of the negative electrode L_- is determined by the thickness of the positive electrode L_+, the volume fractions of electroactive material in each electrode ϵ_i, the accessible capacity of each electrode material Δc_i, and the excess negative electrode capacity γ. Here $1+\gamma$ is the ratio of the negative to positive electrode capacities.

$$L_- = (1+\gamma) \frac{\Delta c_+ \epsilon_+}{\Delta c_- \epsilon_-} L_+ \quad [B21]$$

The simulations are parameterized using the parameters SOH (state of health) and SOC (state of charge) to determine initial solid phase lithium concentrations in the electrode. The SOH is defined as the available cycleable lithium inventory contained in the cell normalized by the initial cycleable lithium inventory contained in the cell at $SOH = 1$. It is assumed that the initial lithium inventory is set solely by the positive electrode, which is valid for cells constructed from negative electrode materials that do not contain cycleable lithium (e.g. graphite or silicon), which leads to Eq. B22.

$$SOH = \frac{(c_{+,ave} - c_{+,min})}{\Delta c_+} + \frac{(c_{-,ave} - c_{-,min})}{\Delta c_-}(1+\gamma) \quad [B22]$$

The SOC is defined as the cycleable lithium contained in the negative electrode normalized by the total cycleable lithium contained in the system at a given SOH, which can be expressed as

$$SOC = \frac{(c_{-,ave} - c_{-,min})(1+\gamma)}{(\Delta c_-) SOH} \quad [B23]$$

The above definitions of SOH and SOC show that the average solid phase concentration of lithium ($c_{s,ave}$) in each electrode can be specified using the SOC and SOH parameters, as $c_{s,min}$, Δc_s, and γ are fixed by the electrode materials and cell design.

Appendix C: Concentration Dependent Parameters

The concentration and temperature dependent properties based on those used in Ref. 36 for the lithium-ion cell considered in this work are expressed below and plotted in Fig. C1. Note that all temperature dependent relations are evaluated at $T = 298K$.

The salt-diffusion coefficient and conductivity of the bulk electrolyte used in this work taken from Ref. 50 are reproduced below. These are the same relations used in the cell modeled in Ref. 36.

$$D_{l,bulk} = 10^{-8.43 - 54/(T - 0.005 c_l - 229) - 2.2 \cdot 10^{-4}} \quad [C1]$$

$$\kappa_{l,bulk} = 10^{-4} c_l (-10.5 + 0.074T - 6.96 \cdot 10^{-5} T^2 + 6.68 \cdot 10^{-4} c_l - 1.78 \cdot 10^{-5} c_l T + 2.8 \cdot 10^{-8} c_l T^2 + 4.94 \cdot 10^{-7} c_l^2 T) \quad [C2]$$

The empirical relation for v is based on empirical relations for v published in Ref. 50 and altered to match the plot of v presented in Refs. 36 and 37:

$$v = 0.601 - 0.24 \left(\frac{c_l}{1000} \right)^{0.5} + 0.982\,(1 - 0.0052\,(T - 294)) \left(\frac{c_l}{1000} \right)^{1.5} \quad [C3]$$

The diffusion coefficient of lithium in graphite is based on the empirical relation reported in Ref. 36 and is reproduced below.

$$D_{s,-} = 1.4523 \cdot 10^{13} \exp\left(\frac{68025.7}{R} \left(\frac{1}{318} - \frac{1}{T} \right) \right) \quad [C4]$$

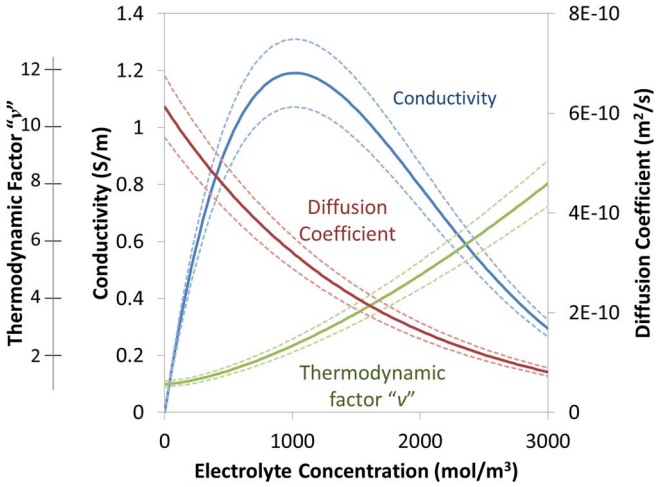

Figure C1. Plots of the concentration dependent parameters used in this simulation. The dashed lines indicate the +/− 10% values used in the sensitivity analysis.

The empirical relation for the concentration dependent equilibrium potentials of the Li_yCoO_2 and Li_xC_6 electrodes used in this work taken from 26 are reproduced below and plotted in Fig. C2.

$$U_+ = 3.8552 + 1.2473\,(1-y) - 11.152\,(1-y)^2 + 42.8185\,(1-y)^3 - 67.711\,(1-y)^4 + 42.508\,(1-y)^5 - 6.132\cdot 10^{-4}\exp\left(7.657y^{115}\right) \quad [C5]$$

$$U_- = 0.7222 + 0.13868x + 0.028952x^{0.5} - 0.017189x^{-1} + 0.0019144x^{-1.5} + 0.28082\exp\left(15\,(0.06-x)\right) - 0.78944\exp\left(0.44649\,(x-0.92)\right) \quad [C6]$$

In the sensitivity analysis, the slopes of the equilibrium potential curves $\left(\frac{\partial U_i}{\partial c_s}\right)$ are varied by a factor +/− 0.1 according to this equation.

$$U_i' = (1\pm 0.1)\cdot U_i \mp 0.1\cdot U_i\left(c_{s,4.1V}\right) \quad [C7]$$

The resulting equilibrium potential curves U_i' are plotted in Fig. 10 as dashed lines. It can be verified that the expression in Eq. C7 is equivalent to increasing $\frac{\partial U_i}{\partial c_s}$ for all c_s by taking the derivative of both sides of the equation. The initial conditions are chosen such that U_+ and U_- have the same values at $y = 0.42$ and $x = 0$, respectively, to reduce alteration of the voltage cutoff at end of charge.

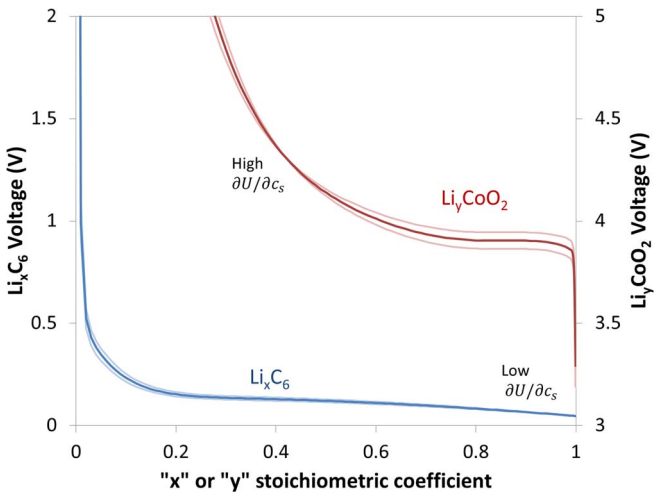

Figure C2. Plots of the equilibrium potentials of the positive and negative electrodes used in this work. The dashed lines indicate the +/− 10% values used in the sensitivity analysis.

References

1. Z. Li, J. Huang, B. Yann Liaw, V. Metzler, and J. Zhang, *Journal of Power Sources*, **254**, 168 (2014).
2. D. Aurbach, E. Zinigrad, Y. Cohen, and H. Teller, *Solid State Ionics*, **148**, 405 (2002).
3. J. Cannarella and C. B. Arnold, *Journal of Power Sources*, **245**, 745 (2014).
4. M. Klett, R. Eriksson, J. Groot, P. Svens, K. C. Högström, R. W. Lindström, H. Berg, T. Gustafson, G. Lindbergh, and K. Edström, *Journal of Power Sources*, **257**, 126 (2014).
5. E. Sarasketa-Zabala, F. Aguesse, I. Villarreal, L. M. Rodriguez-Martinez, C. M. López, and P. Kubiak, *The Journal of Physical Chemistry C*, **119**, 896 (2015).
6. S. J. Harris and P. Lu, *The Journal of Physical Chemistry C*, **117**, 6481 (2013).
7. J. Vetter, P. Novák, M. Wagner, C. Veit, K.-C. Möller, J. Besenhard, M. Winter, M. Wohlfahrt-Mehrens, C. Vogler, and a. Hammouche, *Journal of Power Sources*, **147**, 269 (2005).
8. N. Zhang and H. Tang, *Journal of Power Sources*, **218**, 52 (2012).
9. P. Arora, R. E. White, and M. Doyle, *Journal of the Electrochemical Society*, **145**, 3647 (1998).
10. D. Kehrwald, P. R. Shearing, N. P. Brandon, P. K. Sinha, and S. J. Harris, *Journal of The Electrochemical Society*, **158**, A1393 (2011).
11. J. Schmitt, F. Treuer, F. Dietrich, K. Dröder, T.-P. Heins, U. Schröder, U. Westerhoff, M. Kurrat, and A. Raatzauthor, 2014, pp. 395–400.
12. T. Waldmann, S. Gorse, T. Samtleben, G. Schneider, V. Knoblauch, and M. Wohlfahrt-Mehrens, *Journal of the Electrochemical Society*, **161**, A1742 (2014).
13. E. Sahraei, J. Meier, and T. Wierzbicki, *Journal of Power Sources*, **247**, 503 (2014).
14. C. Peabody and C. B. Arnold, *Journal of Power Sources*, 2011, 8147
15. J. Cannarella, C. Z. Leng, and C. B. Arnold, *Proc. of SPIE*, **9115**, 91150K (2014).
16. K.-Y. Oh, J. B. Siegel, L. Secondo, S. U. Kim, N. a. Samad, J. Qin, D. Anderson, K. Garikipati, A. Knobloch, B. I. Epureanu, C. W. Monroe, and A. Stefanopoulou, *Journal of Power Sources*, **267**, 197 (2014).
17. S. Mohan, Y. Kim, J. B. Siegel, N. a. Samad, and a. G. Stefanopoulou, *Journal of the Electrochemical Society*, **161**, A2222 (2014).
18. R. Fu, M. Xiao, and S.-Y. Choe, *Journal of Power Sources*, **224**, 211 (2013).
19. J. Cannarella and C. B. Arnold, *Journal of Power Sources*, **269**, 7 (2014).
20. E. M. C. Jones, M. N. Silberstein, S. R. White, and N. R. Sottos, *Experimental Mechanics*, **54**, 971 (2014).
21. a. Matasso, D. Wetz, and F. Liu, *Journal of the Electrochemical Society*, **162**, A92 (2014).
22. J. Cannarella and C. B. Arnold, *Journal of Power Sources*, **226**, 149 (2013).
23. Y. Pan and Z. Zhong, *Journal of the Electrochemical Society*, **161**, A583 (2014).
24. W. Wu, X. Xiao, X. Huang, and S. Yan, *Computational Materials Science*, **83**, 127 (2014).
25. D. Antartis, S. Dillon, and I. Chasiotis, *Journal of Composite Materials*, (2015).
26. M. Tang, P. Albertus, and J. Newman, *Journal of The Electrochemical Society*, **156**, A390 (2009).
27. P. Arora, M. Doyle, and R. E. White, *J. Electrochem. Soc.*, **146**, 3543 (1999).
28. S. Zhang, K. Xu, and T. Jow, *Journal of Power Sources*, **160**, 1349 (2006).
29. M. Petzl and M. a. Danzer, *Journal of Power Sources*, **254**, 80 (2014).
30. S. J. Harris, A. Timmons, D. R. Baker, and C. Monroe, **485**, 265 (2010).
31. M. Zier, F. Scheiba, S. Oswald, J. Thomas, D. Goers, T. Scherer, M. Klose, H. Ehrenberg, and J. Eckert, *Journal of Power Sources*, **266**, 198 (2014).
32. H. Honbo, K. Takei, Y. Ishii, and T. Nishida, *Journal of Power Sources*, **189**, 337 (2009).
33. T. F. Fuller, M. Doyle, and J. Newman, *Journal of The Electrochemical Society*, **141**, 1 (1994).
34. M. Doyle, T. Fuller, and J. Newman, *Journal of The Electrochemical Society*, **140**, year (1993).
35. R. D. Perkins, A. V. Randall, X. Zhang, and G. L. Plett, *Journal of Power Sources*, **209**, 318 (2012).
36. K. Kumaresan, G. Sikha, and R. E. White, *Journal of The Electrochemical Society*, **155**, A164 (2008).
37. S. Renganathan, G. Sikha, S. Santhanagopalan, and R. E. White, *Journal of The Electrochemical Society*, **157**, A155 (2010).
38. C. Uhlmann, J. Illig, M. Ender, R. Schuster, and E. Ivers-Tiffée, *Journal of Power Sources*, **279**, 428 (2015).
39. B. Bitzer and A. Gruhle, *Journal of Power Sources*, **262**, 297 (2014).
40. T. Waldmann, M. Wilka, M. Kasper, M. Fleischhammer, and M. Wohlfahrt-Mehrens, *Journal of Power Sources*, **262**, 129 (2014).
41. B. Sood, M. Osterman, and M. PechtProduct Compliance Engineering (ISPCE), 2013 IEEE Symposium on, 2013, pp. 1–6
42. S. Bhadra, A. Hsieh, B. J. Hertzberg, P. J. Gjeltema, and D. A. Steingart, *Energy Environ. Sci.*, (2015).
43. M. Ebner, D.-W. Chung, R. E. García, and V. Wood, *Advanced Energy Materials*, 2014, **4**.
44. I. V. Thorat, D. E. Stephenson, N. a. Zacharias, K. Zaghib, J. N. Harb, and D. R. Wheeler, *Journal of Power Sources*, **188**, 592 (2009).
45. J. Cannarella, X. Liu, C. Z. Leng, P. D. Sinko, G. Y. Gor, and C. B. Arnold, *Journal of the Electrochemical Society*, **161**, F3117 (2014).
46. G. Y. Gor, J. Cannarella, J. H. Prevost, and C. B. Arnold, *Journal of the Electrochemical Society*, **161**, F3065 (2014).
47. S. Yan, X. Xiao, X. Huang, X. Li, and Y. Qi, *Polymer*, **55**, 6282 (2014).
48. I. Avdeev, M. Martinsen, and A. Francis, *Journal of Materials Engineering and Performance*, **23**, 315 (2014).
49. A. Sheidaei, X. Xiao, X. Huang, and J. Hitt, **196**, 8728 (2011).
50. L. O. Valoen and J. N. Reimers, *Journal of The Electrochemical Society*, **152**, A882 (2005).